Risk Topology Construction Method of Flight Manipulation in Turbulent-Windshear Conditions Based on Multivariate Copula Theory

GUOZHI WANG[ID], HAOJUN XU[ID], BINBIN PEI, YUAN XUE, AND XIAOCONG DUAN

Aeronautics Engineering College, Air Force Engineering University, Xi'an 710038, China

Corresponding author: Yuan Xue (szxy1986@163.com)

ABSTRACT Complex weather conditions, especially turbulent-windshear conditions, have severe effects on the landing safety of an aircraft. Based on a distributed human-machine-environment real-time simulation system, virtual landing simulations in turbulent-windshear conditions were carried out using the Monte Carlo method. By analyzing the simulation results, it was determined that the flight parameters that significantly affect the landing safety of an aircraft are the sideslip angle β, descent height ΔH, and angle of attack α. Based on multivariate copula theory, the statistical characteristics of the extreme values of the flight parameters were analyzed, the unknown parameters in the distribution models were identified, and the goodness of fit was tested. The risk of landing in turbulent-windshear conditions was quantitatively evaluated. By applying the quantitative risk evaluation method proposed in this study, the risk topology of flight manipulation for landing in turbulent-windshear conditions was constructed using the pitch angle variation $\Delta\theta$, yaw angle variation $\Delta\psi$, and flight distance L. The risk topology can not only greatly improve the situational awareness of the pilot but also provide comprehensive and intuitive guidance for removing aircraft from the impacts of wind-shear.

INDEX TERMS Complex system simulation, Monte Carlo method, turbulent-windshear, multivariate copula theory, manipulation risk topology.

I. INTRODUCTION

The takeoff and landing time of an aircraft only account for 5% of the overall flight time, but 48% of the flight accidents occur during this period. The lack of situational awareness and flight manipulation errors caused by turbulent-windshear conditions account for 66% of the accidents [1]. When an aircraft encounters turbulent-windshear during a landing approach, the sharply changing wind vector will induce a sharp change in the lift. Consequently, the aircraft attitude and flight trajectory will deviate from the predetermined state, which will directly endanger the flight safety. In 2009, FedEx Flight 80 crashed due to turbulent-windshear when landing at Narita International Airport, Japan [2]. In 2012, Bhoja Air Flight BH023 took off at the Karachi Jinnah International Airport and suffered from windshear. Unfortunately, because

the flight crew failed to recover from the stall, the aircraft crashed [2].

Civil aircraft not only must ensure flight safety but also must maximize the economic benefits. Hence, the optimization of flight control strategies across a wide array of complex flight conditions has been a popular research objective for many years. Automatic landing systems were developed to achieve robust accurate tracking in the presence of windshear, using the stable inversion control method [3]. An optimal feedback control strategy based on the viability theory for improving the aircraft control capabilities during cruise phase in wind shear conditions [4]. The disturbance attenuation control of an aircraft flying through windshear was achieved via linear parameter varying (LPV) model and a control method [5].

All the flight control strategies described above are effective in the presence of windshear with middle/low intensity, but may fail in the presence of wind shear with high intensity.

The associate editor coordinating the review of this manuscript and approving it for publication was Xin Luo[ID].

The failure of control strategies under complex flight conditions means that the aircraft cannot recovery from a dangerous attitude which can result in a flight accident. Hence, it was asserted that once windshear is encountered, to keep the aircraft attitude stable, the best choice of the crew is to escape quickly [6]. Determining how to improve situational awareness and reduce flight manipulation errors in complex flight conditions is a key issue. The flight-safety space proposed previously greatly enhanced the pilot's ability to avoid placing the aircraft in a dangerous flight situation [7]. This study focused on the risk topology construction method of flight manipulation in turbulent-windshear conditions to provide intuitive and predictive information to the crew.

The rest of this paper is organized as follows. Section II introduces multivariate copula theory and the process of virtual flight simulation that based on Monte Carlo method. Section III presents operation model and environment model in detail. The turbulent-windshear model is optimized by combining *n* ring-vortex models and Dryden model. Section IV shows the analysis of simulation results obtained from the virtual landing simulation under turbulent-windshear conditions, it was determined that the flight parameters that significantly affect the landing safety of an aircraft are the sideslip angle β, descent height ΔH, and angle of attack α. Section V presents risk evaluation model based on multivariate copula theory. The distributions of the one-dimensional extreme values of the flight parameters were fitted first, and goodness-of-fit tests (Kolmogorov-Smirnov (K-S) test, Anderson-Darling test, and chi-squared (χ^2) test) were used to test the data distributions, and it was confirmed that the generalized extreme value (GEV) distribution model could describe the one-dimensional distributions more effectively. The three-dimensional copula function C that describes the correlations between the three-dimensional parameters, was confirmed by using goodness-of-fit tests (Akaike Information Criteria (AIC), Bayesian Information Criteria (BIC), χ^2 test, and K-S test). To improve the flexibility and accuracy, three-dimensional copula models that achieved high goodness-of-fit values, were used to compose the risk-weighted model, and the risk of landing in turbulent-windshear conditions was quantitatively evaluated. Section VI shows the risk topology of flight manipulation for landing in turbulent-windshear conditions, which is constructed using the pitch angle variation $\Delta\theta$, yaw angle variation $\Delta\psi$, and flight distance L. The risk-evolution mechanism of flight manipulation for landing in turbulent-windshear conditions was analyzed in detail. Section VII draws important conclusions.

This work contributes to communities of flight manipulation envelope and risk-evolution mechanism analysis in the following aspects: 1) a turbulent-windshear model was developed by combining n ring-vortex models and Dryden model, which can simulate a real windshear environment and satisfy risk evaluation requirements. 2) a risk-weighted model was proposed to improve the efficiency of risk evaluation and reduce the number of virtual flight simulation times.

3) a risk topology construction method of flight manipulation was proposed in this study combines complex system simulations with quantitative risk assessment from a global perspective. 4) the risk-evolution mechanism was analyzed in detail, which provides some insights into the performance of aircraft in turbulent-windshear conditions.

Compared with flow field information of turbulent-windshear conditions, the information provided by the risk topology is more valuable. Because it allows the pilot to determine the manipulation strategies in turbulent-windshear conditions. The results of this work suggest that the risk topology construction method of flight manipulation can serve as an effective auxiliary means for the pilot to keep an aircraft in the safety zone under turbulent-windshear conditions.

II. COMPUTATIONAL THEORY AND METHOD
A. MULTIVARIATE COPULA THEORY
It is supposed that a sequence of random variables $\{X_n\}$ is independent, its distribution function is $F(x)$, and its maximum array $M_n = \max\{X_1, \cdots, X_n\}$. A sequence exists $\{a_n > 0\}, \{b_n\}$ such that

$$P\left(\frac{M_n - b_n}{a_n} \leq x\right) \xrightarrow{d} F^*(x), \quad (1)$$

where $F^*(x)$ is an extreme distribution function, $\xrightarrow{d}$ represents weak convergence, b_n is the positional parameter, $-\infty < b_n < +\infty$, and a_n indicates the dispersion degree of the data, $a_n > 0$.

The distributions of the sample extreme parameters are independent of the distribution of the sample data, which is an important feature of extreme value theory. Hence, quantitative assessment of the flight risk can be achieved by extracting the extreme values of the flight parameters and determining the distribution functions of the extreme parameters. However, for flight safety assessment in turbulent-windshear conditions, risk occurrence is affected by many factors, which means that the risk event function $F(x_1, \cdots, x_n)$ is composed of *n* variables. Based on Sklar's theorem, the risk event function $F(x_1, \cdots, x_n)$ is separated into two parts:

(1) *n* edge distribution functions $F_1(x_1), \cdots, F_n(x_n)$, which describe the distribution characteristics of *n* extreme parameter variables;

(2) the multivariate copula function $C(\cdot)$, which describes the correlation between *n* extreme parameter variables.

$$F(x_1, \cdots, x_n) = C(F_1(x_1), \cdots, F_n(x_n)), \quad (2)$$

where $\forall x \in \tilde{R}^n, \tilde{R} \cup \{\pm\infty\}$.

Letting $u_i = F_i(x_i)$, $u_i \in [0, 1]$, $i = 1, \cdots, n$ an N-dimensional copula function can be described as follows:

$$\begin{aligned} C(u_1, \cdots, u_n) &= P(U_1 \leq u_1, \cdots, U_n \leq u_n) \\ &= F\left(F_1^{-1}(u_1), \cdots, F_n^{-1}(u_n)\right), \quad (3) \end{aligned}$$
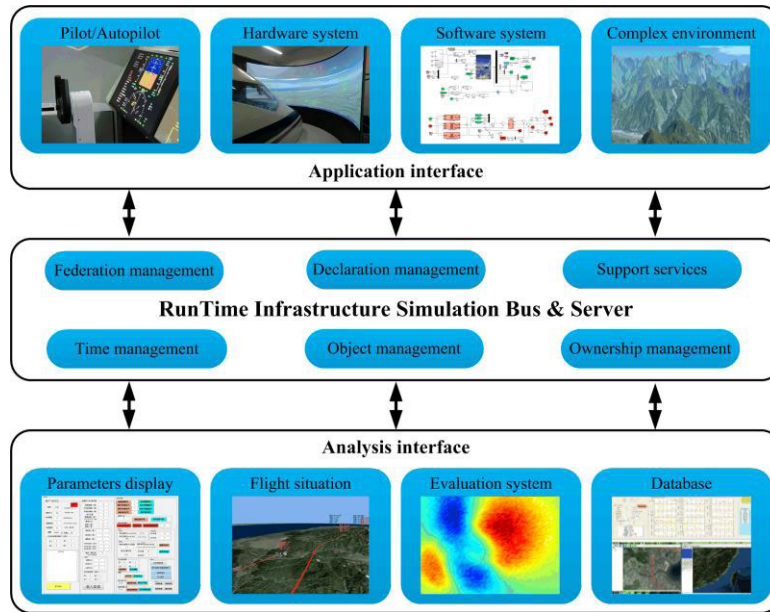
FIGURE 1. Distributed pilot-machine-environment real-time simulation system based on the HLA standard.

The N-dimensional probability density function is as follows:

$$f(x_1, \cdots, x_n) = \frac{\partial C^n (u_1, \cdots, u_n)}{\partial u_1 \cdots \partial u_n} \prod_{i=1}^{n} f_i(x_i). \qquad (4)$$

where $f_i(x_i)$ is the probability density function of the edge distribution function $F_i(\cdot)$.

B. MONTE CARLO METHOD

Using multivariate copula theory to estimate the flight risk, a large amount of flight data obtained in turbulent-windshear conditions is required. However, real flight data obtained in turbulent-windshear conditions is too rare to be adequate for quantitative risk assessment model construction. Moreover, the flight tests in turbulent-windshear conditions are harsh, and the flight risk is great. Hence, a distributed pilot-machine-environment real-time simulation system is constructed in this study, which is based on the High Level Architecture (HLA) standard [8], as shown in Figure 1. The system has the advantages of a shorter time delay and better scalability. It can provide data for the quantitative assessment of flight risk as well as a system support for flight training in the case of turbulent-windshear.

Based on Monte Carlo method, environmental parameters and operation characteristic parameters were sampled, as shown in Table 1, and they were input to the distributed pilot-machine-environment real-time simulation system. n virtual flight simulations were carried out. The process of virtual flight simulation is illustrated in Figure 2. A large amount of flight parameter data that can reflect the dynamic response characteristics of the pilot-machine-environment

TABLE 1. Sampled parameter variables.

Environmental parameters	Operation characteristic parameters
1) Vortex intensity	1) Static gain
2) Vortex axis angle	2) Reaction time delay
3) Vortex-ring radius	3) System time-delay parameter
4) Vortex-core radius	4) Pre-operation parameter
	5)Musculonervous system parameter

complex system under turbulent-windshear conditions was obtained.

The process of virtual flight simulation based on the Monte Carlo method was as follows:

Step 1: Initialize. Set flight altitude, airspeed, glide angle, and virtual flight simulation times n;

Step 2: Sample. Sample environmental model parameters and operation model characteristic parameters;

Step 3: Simulate. Perform the ith iterative flight simulation;

Step 4: Data processing. Extract flight parameter extrema. Record and store the flight parameters in the ith iterative simulation. Then, extract the flight parameter extrema and store them in a database;

Step 5: Set $i = i + 1$. Return to Step 2 and continue the simulation until $i > n$.

III. SIMULATION MODEL
A. OPERATION MODEL
Based on the study of pilot operation behaviors [9], the following operation model $Y_P(s)$ is proposed:

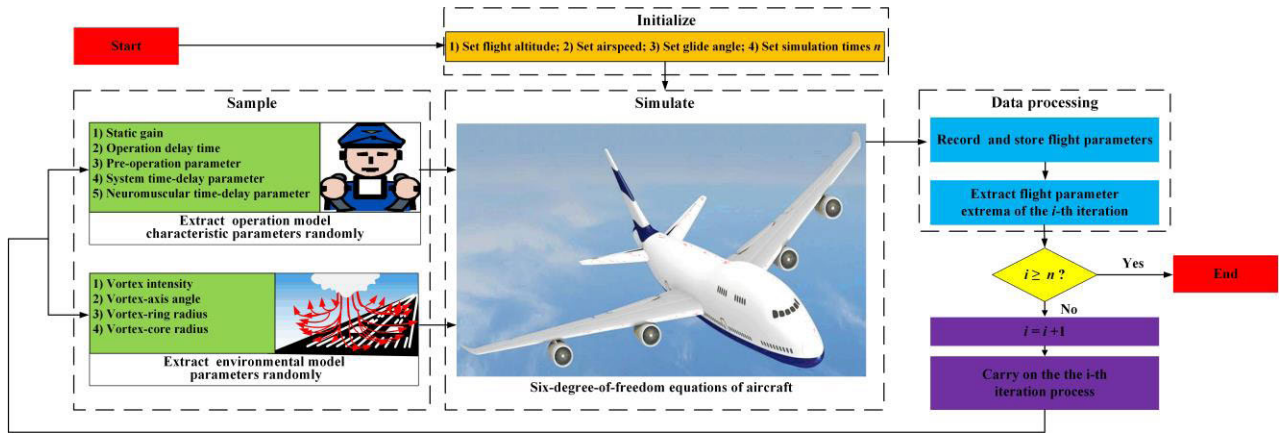$$Y_P(s) = Y_A(s) \bullet Y_N(s), \qquad (5)$$

FIGURE 2. Process of virtual flight simulation based on Monte Carlo method.

where $Y_A (s)$ is an adaptive transfer function of the operation model, which is mainly composed of the operation behavior parameters τ, k_p, T_1, T_2, and reflects the pilot's use of the stick to control the motion attitude of the aircraft. It can be expressed as follows:

$$Y_A (s) = \frac{k_p e^{-\tau s} (T_1 s + 1)}{T_2 s + 1}, \qquad (6)$$

where τ is the operation delay time, $\tau \subset [0.06, 0.3]$; k_p is the static gain, $k_p \geq 1$; T_1 is the pre-operation parameter, $T_1 \subset (0, 1]$; and T_2 is the system time-delay parameter, $T_2 \subset (0, 1]$.

$Y_N (s)$ is the pilot's neuromuscular system function, which is expressed as follows:

$$Y_N (s) = \frac{(T_N s + 1) \omega_n^2}{(0.1s + 1)^2 (s^2 + 2\xi_n \omega_n s + \omega_n^2)}, \qquad (7)$$

where T_N is the neuromuscular system time-delay parameter, $\omega_n = 16.5 \text{rad/s}$ is the undamped natural frequency, and $\xi_n = 0.12$ is relative damping coefficient.

TABLE 2. Sampling results of operation characteristic parameters.

Parameter	k_p	τ	T_1	T_2	T_N
Results	2.256	0.172	0.226	0.236	0.130

In an actual project, there are differences between the operations of different pilots. The differences are simulated by randomly sampling the operation characteristic parameters τ, k_p, T_1, T_2, T_N. It is assumed that the operation characteristic parameters τ, k_p, T_1, T_2, T_N follow truncated normal distributions. The sampling results are shown in Table 2.

Substituting the sampling results into Eq.(5), the operation model can be expressed as follows:

$$Y_p (s) = \frac{2.256 e^{-0.172s} (0.226s + 1)}{0.236s + 1}$$
$$\bullet \left[\frac{(0.13s+1) \times 16.5^2}{(0.1s+1)^2 (s^2 + 024 \times 16.5s + 16.5^2)} \right]. \qquad (8)$$

When inputting the step signal, the simulation results were basically consistent with the actual operations of pilots, which is shown in Figure 3.
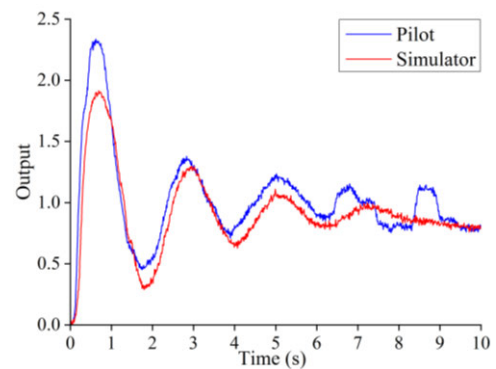

FIGURE 3. Simulation result when inputting the step signal.

B. TURBULENT-WINDSHEAR MODEL

There is a growing amount of literature on methods for modeling windshear and their application to flight simulations. The Joint Airport Weather Studies (JAWS) Project proposed the JAWS model based on data sets that were measured by Doppler radar [10]. A ring-vortex model based on hydrodynamics was developed for real-time flight simulations of takeoffs and landings [11]. Furthermore, the windshear model employed in previous studies [12]–[14] relied

TABLE 3. Multi-vortex composite model characteristic parameters.

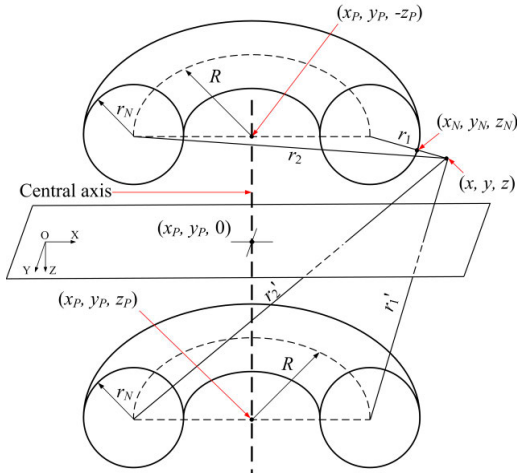| Multi-vortex composite	Vortex center	Vortex intensity Γ m/s²	Vortex-axis angle $[\phi^w, \theta^w, \varphi^w]$ °	Vortex-ring radius R m/s	Vortex-core radius r_N m/s
1	2500,3200,700	⁻7000,⁻9000	$[\ 10,20\ ,\ ^-25,^-15\ ,\ 5,15\ ]$	600,700	300,350
2	2800,2800,900	15000,17000	$[\ 15,25\ ,\ 5,15\ ,\ 10,20\ ]$	800,1000	400,500
3	5000,4500,800	8000,11000	$[\ 5,15\ ,\ 20,30\ ,\ 0,10\ ]$	850,950	400,450

FIGURE 4. Ring-vortex model.

on the Soesman model to study the optimization of windshear recovery trajectory. The performances of candidate windshear detection devices were investigated using the Bowles-Oseguera model to simulate wind shear conditions [15]. All the models described above have the same problem: the simulated flow field is axisymmetric. However, the flow field, which is affected by turbulence, the wake, and ground obstacles, is non-axisymmetric in real windshear conditions. Hence, the turbulent-windshear model was built based on ring-vortex and Dryden models [16], which could reflect the non-axisymmetric characteristics of the flow field.

$$
u_t = \begin{cases} \lambda \cdot \left(\dfrac{x_N - x_p}{r_N^2} \right) \left. \dfrac{\partial \psi_t}{\partial z} \right|_N & 0 < \lambda < 1 \\[2ex] \left(\dfrac{x - x_p}{r^2} \right) \dfrac{\partial \psi_t}{\partial z} & \lambda > 1 \end{cases}
$$

$$
v_t = \begin{cases} \lambda \cdot \left(\dfrac{y_N - y_p}{r_N^2} \right) \left. \dfrac{\partial \psi_t}{\partial z} \right|_N & 0 < \lambda < 1 \\[2ex] \left(\dfrac{y - y_p}{r^2} \right) \dfrac{\partial \psi_t}{\partial z} & \lambda > 1 \end{cases}
$$

$$
w_t = \begin{cases} \lambda \cdot \left(-\dfrac{1}{r_N} \right) \left. \dfrac{\partial \psi_t}{\partial r} \right|_N & 0 < \lambda < 1 \\[2ex] \left(-\dfrac{1}{r} \right) \dfrac{\partial \psi_t}{\partial r} & \lambda > 1, \end{cases} \tag{9}
$$

where $\psi_t = \psi_t (r, z, \Gamma)$ is the expression of a vortex circulation line equation [17], r is the distance between the reference mass (x, y, z) and the ring-vortex axis, the minimum distance is r_1, the maximum distance is r_2, and $\lambda = r_1/r_N$ is the proportionality coefficient.

The simulation precision for the windshear filed was improved by additional optimization. The expression of the turbulent-windshear model is as follows:

$$
W = \begin{bmatrix} W_x \\ W_y \\ W_z \end{bmatrix} = \begin{bmatrix} W_{xw} \\ W_{yw} \\ W_{zw} \end{bmatrix} + \begin{bmatrix} W_{xt} \\ W_{yt} \\ W_{zt} \end{bmatrix} \tag{10}
$$

where $\begin{bmatrix} W_{xw} & W_{yw} & W_{zw} \end{bmatrix}^T$ is a function of the velocity field formed by Dryden model, and $\begin{bmatrix} W_{xt} & W_{yt} & W_{zt} \end{bmatrix}^T$ is a function of the velocity field formed by n vortex-rings.

$\begin{bmatrix} W_{xw} & W_{yw} & W_{zw} \end{bmatrix}^T$ can be easily obtained using commercial software (MATLAB). $\begin{bmatrix} W_{xt} & W_{yt} & W_{zt} \end{bmatrix}^T$ can be calculated as follows:

$$
\begin{bmatrix} W_{xt} \\ W_{yt} \\ W_{zt} \end{bmatrix} = L(\phi_1^w, \theta_1^w, \psi_1^w) \begin{bmatrix} u_t^1 \\ v_t^1 \\ w_t^1 \end{bmatrix} + \cdots
$$
$$
+ L(\phi_n^w, \theta_n^w, \psi_n^w) \begin{bmatrix} u_t^n \\ v_t^n \\ w_t^n \end{bmatrix}. \tag{11}
$$

where $[\phi^w, \theta^w, \psi^w]$ is the angle between the central axis of the ring-vortex and the ground. The transformation matrix $L(\phi^w, \theta^w, \psi^w)$ can be expressed as follows:

$$
L(\phi^w, \theta^w, \psi^w) = \begin{bmatrix} 1 & 0 & 0 \\ 0 & \cos \phi^w & \sin \phi^w \\ 0 & -\sin \phi^w & \cos \phi^w \end{bmatrix}
$$
$$
\cdot \begin{bmatrix} \cos \theta^w & 0 & -\sin \theta^w \\ 0 & 1 & 0 \\ \sin \theta^w & 0 & \cos \theta^w \end{bmatrix}
$$
$$
\cdot \begin{bmatrix} \cos \psi^w & \sin \psi^w & 0 \\ -\sin \psi^w & \cos \psi^w & 0 \\ 0 & 0 & 1 \end{bmatrix}. \tag{12}
$$

As this study focused on the risk topology construction method of flight manipulation, some turbulent-windshear model parameters were varied, and their variation had significant effects on the flight.

It is assumed that the multi-vortex composite model characteristic parameters as shown in Table 3, vortex intensity Γ,
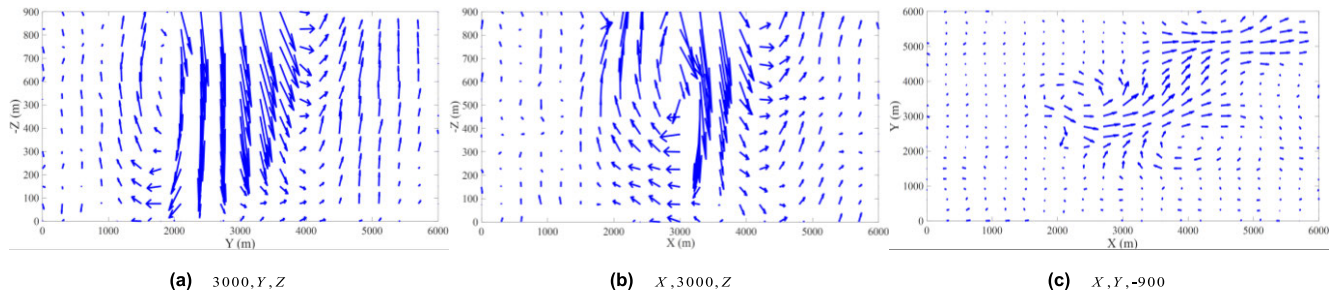
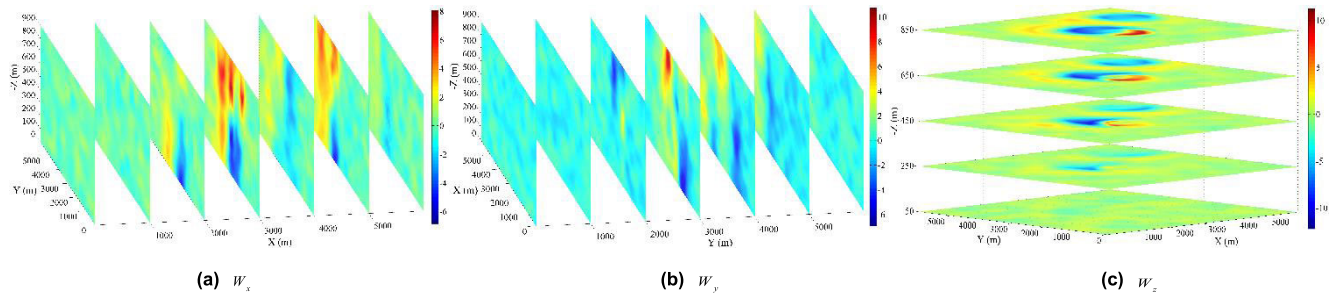**FIGURE 5.** Streamline diagram of turbulent-windshear.

FIGURE 6. Wind speed vector *W* diagram of turbulent-windshear.

vortex-axis angle $[\phi^w, \theta^w, \psi^w]$, vortex-ring radius R, and vortex-core radius r_N follow truncated normal distributions within well-defined intervals.

In the simulation process, the characteristic parameters of the multi-vortex composite model were randomly sampled to construct the turbulent-windshear field. Its streamline diagram is shown in Figure 5, and the wind speed vector W is shown in Figure 6.

Considering the coupling effect of the turbulent-windshear condition, the turbulent-windshear model constructed in this paper can simulate a real windshear environment well and satisfy risk evaluation requirements.

IV. RISK PARAMETERS AND BOUNDARY ANALYSIS

Following Step 1 for the process of virtual flight simulation described above, the initial simulation states were established. The initial main parameters of the aircraft are shown in Table 4.

TABLE 4. Initial main parameters of the aircraft.

Parameter	Value
Airspeed V	75 m/s
Altitude H	450 m
Glide angle	$-3°$
Angle of attack α	$2°$
Sideslip angle β	$0°$
Roll angle ϕ	$0°$
Pitch angle θ	$-1°$
Yaw angle ψ	$0°$

Figure 7 shows the flight parameters of the 200th simulation iteration. The airspeed V and altitude H showed slight decreases. This was because the headwind affected the aircraft initially and resulted in an increase in the aircraft lift. Hence, the engine thrust decreased to allow the flight trajectory to remain on the predetermined glide trajectory. Then, the sideslip angle β of the aircraft influenced by the lateral airflow began to increase. A moment later, the aircraft entered the downdraft, and the angle of attack α of the aircraft decreased. Therefore, the aircraft lift decreased sharply, and the aircraft began to lose altitude simultaneously. Due to the drastic changes of the aircraft attitude, the thrust along the x-axis component decreased sharply. The flight speed was further reduced. As the throttle increased and aircraft attitude was adjusted, the airspeed V of the aircraft increased quickly. Furthermore, it is shown in Figure 7(c) that the sideslip angle β exhibited a small increase. This was because the lateral airflow affected the aircraft.

According to the above analysis, the slideslip angle β, angle of attack α, and altitude were more susceptible to turbulent-windshear than the other flight parameters. Hence, the slideslip angle β, angle of attack α, and descent height (within 20 s) ΔH were selected as risk factors. The extracted extreme parameters of the 200th simulation are shown in Table 5.

The formula to determine whether the flight risk is defined as follows:

$$P_r = 1 \; if \; \begin{cases} \beta_{\max} > \beta_c \left(W, Ma\right) \\ \Delta H_{\max} > \Delta H_c \left(b, \phi, \theta, 20\right) \\ \alpha_{\max} > \alpha_c \left(\delta_f, Ma\right). \end{cases} \quad (13)$$

(a) Altitude H

(b) Airspeed V

(c) Angle of attack and sideslip angle α, β
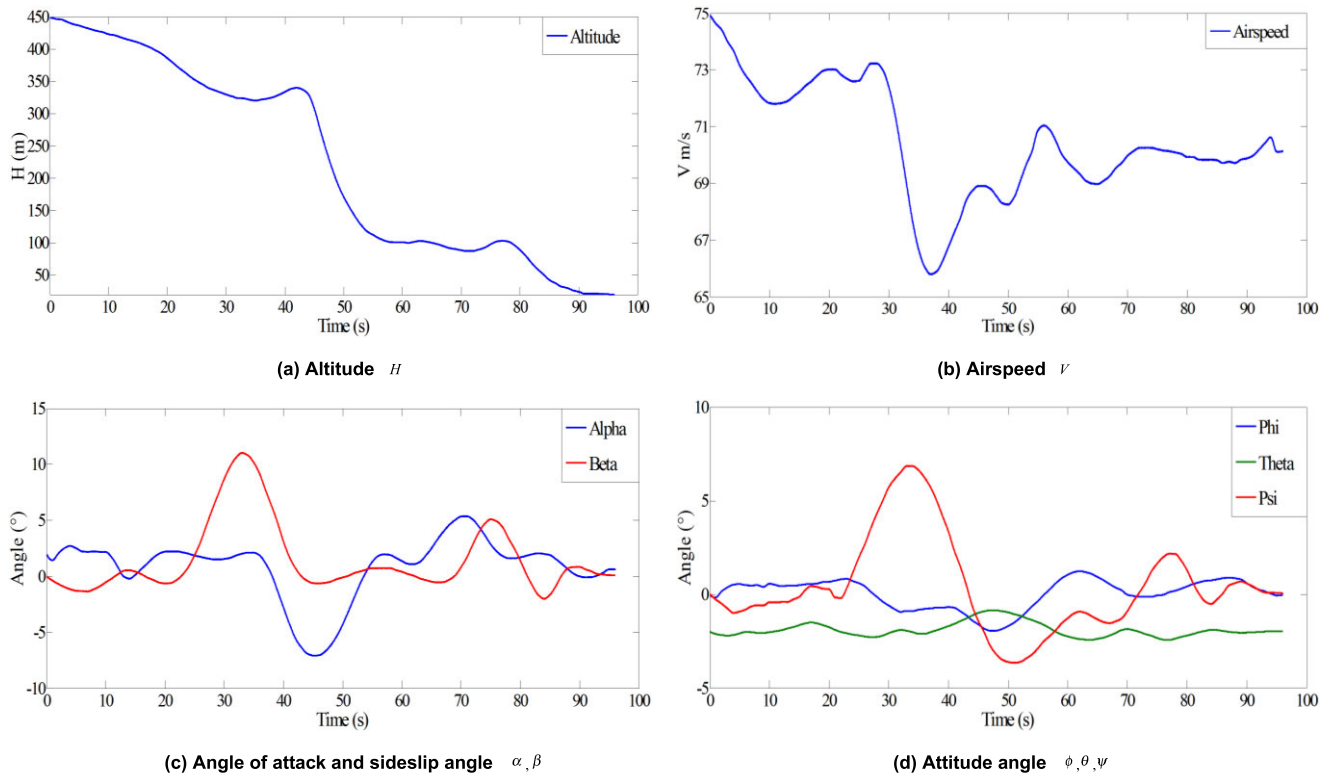
(d) Attitude angle ϕ, θ, ψ

FIGURE 7. Flight parameters of the 200th iterative simulation.

TABLE 5. Extracted extreme flight parameters of the 200th simulation.

Extreme parameter	Sideslip angle	Descent height	Angle of attack
Value	11.0385°	238.662 m	-7.0928°

where $\beta_c\,(W, Ma)$ is the critical sideslip angle, which is related to the Mach number and runway width, $\alpha_c\,(\delta_f, Ma)$ is the critical angle of attack, which is related to the Mach number and flap deflection δ_f, $\Delta H_c\,(b, \phi, \theta, \Delta t)$ is the critical descent height (within 20 s), which is related to the wing length b, roll angle ϕ, and pitch angle θ.

V. BUILD RISK EVALUATION MODEL BASED ON MULTIVARIATE COPULA THEORY

Three hundred virtual landing simulations were performed under turbulent-windshear conditions based on the distributed pilot-machine-environment real-time simulation system. The extreme parameters $[\beta_{max}, H_{max}, \alpha_{max}]$ extracted from the three hundred virtual landing simulations were used as the evaluation data, which are shown in Figure 8. The distributions of the extreme parameters significantly exhibited heavy-tailed characteristics, which is common in high-risk events with low frequencies (e.g., earthquakes, tsunamis, financial risks, and flight accidents [19]–[22]). Multivariate copula theory can be used to study such events effectively,

as it can model the heavy-tailed characteristics of extreme parameter distributions precisely [23]–[29].

Despite the characteristics of extreme parameter distributions are revealed thus far, because of unmodeled dynamics, external disturbances, and inherent variability of a dynamic process, the uncertainty of pilot-machine-environment real-time simulation system represents a major threat to successful risk evaluation. Several theoretical studies provide some useful model estimation and optimization algorithms to maximize estimation accuracy. Bayesian estimation method has been developed and widely applied to nonlinear system state estimation [30]. The dendritic neuron model with effective learning algorithms is developed for approximation, and prediction [31], [32]. A Lyapunov-type theorem is developed to study global well-posedness and asymptotic stability in probability of nonlinear systems [33]. A new method which combines the sparse signal representation technique and fractional lower order statistics is proposed to improve the effectiveness of direction of arrival estimation [34].

A. IDENTIFY DISTRIBUTION MODEL OF ONE-DIMENSIONAL EXTREME PARAMETERS
1) ANALYSIS OF STATISTICAL CHARACTERISTICS FOR ONE-DIMENSIONAL EXTREME PARAMETERS
The statistical characteristics of the extreme parameters $[\beta_{max}, H_{max}, \alpha_{max}]$ are shown in Table 6.
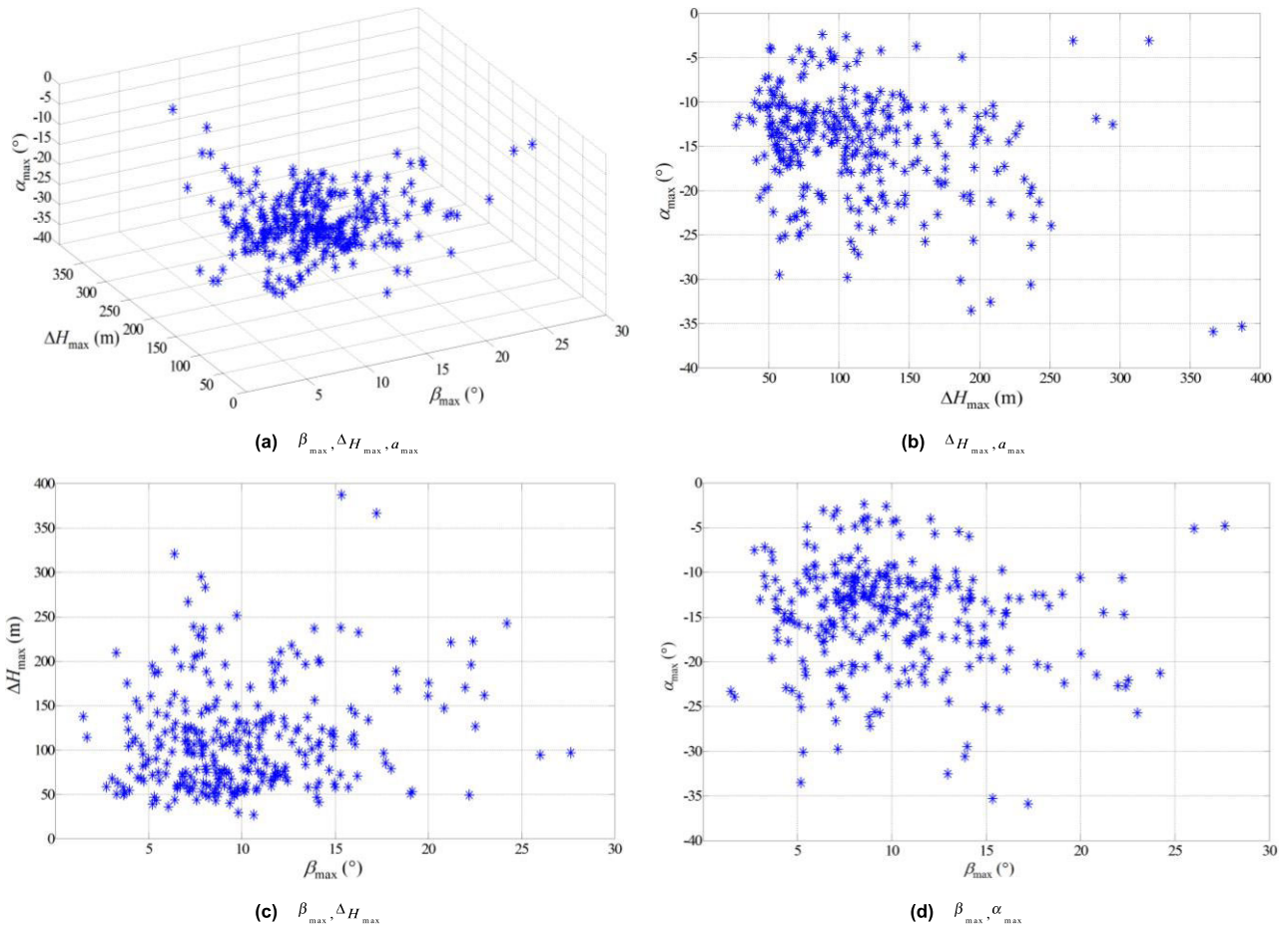
(a) $\beta_{max}, \Delta H_{max}, a_{max}$

(b) $\Delta H_{max}, a_{max}$

(c) $\beta_{max}, \Delta H_{max}$

(d) $\beta_{max}, \alpha_{max}$

FIGURE 8. Three hundred groups of extreme parameters obtained through the simulation.

TABLE 6. Statistical characteristics of the one-dimensional extreme parameters.

Extreme value sample	Minimum value	Maximum value	Mean value	Median	Standard deviation
Sideslip angle	1.477	27.645	9.980	9.152	4.416
Descent height	27.041	386.953	112.860	104.097	58.665
Angle of attack	-35.888	-2.403	-14.718	-13.705	5.898

TABLE 7. Kurtosis and skewness coefficients.

Extreme value sample	Kurtosis coefficient	Skewness coefficient
Sideslip angle	4.575	1.084
Descent height	5.511	1.400
Angle of attack	3.918	-0.884

For the extreme parameters $[\beta_{max}, H_{max}, \alpha_{max}]$, the deviations of the maximum and minimum values from the mean value were asymmetric. Hence, kurtosis (k) and skewness (s) coefficients of the extreme parameter samples were calculated to analyze the extreme parameter distribution features using the following formulas:

$$k = \frac{E(x-\mu)^4}{\sigma^4} = \frac{\frac{1}{n}\sum_{i=1}^{n}(x_i - \bar{x})^4}{\left(\frac{1}{n}\sum_{i=1}^{n}(x_i - \bar{x})^2\right)^2}, \qquad (14)$$

$$s = \frac{E(x-\mu)^3}{\sigma^3} = \frac{\frac{1}{n}\sum_{i=1}^{n}(x_i - \bar{x})^3}{\left(\sqrt{\frac{1}{n}\sum_{i=1}^{n}(x_i - \bar{x})^2}\right)^3}. \qquad (15)$$

The results are presented in Table 7. The kurtosis coefficients of the extreme parameters were all greater than three, which suggested that the distributions of the extreme parameters possessed heavy-tailed characteristics. The skewness coefficients of extreme parameters β_{max}, and ΔH_{max} were greater than zero, which suggested that their heavy-tailed

TABLE 8. Identification results of the unknown parameters.

Distribution Model	F_1 β_{max}	F_2 ΔH_{max}	F_3 α_{max}
GEV	[5.22480, 2.32019, - 0.08931]	38.60043, 17.71067, 0.21725	20.35252, 8.95829, ⁻ 0.07743
Normal	6.38747, 2.70946	53.11015, 28.63823	24.83179, 10.53269
Lognormal	1.75663, 0.46582	3.84401, 0.50391	3.11348, 0.47932
Weibull	7.20744, 2.52892	60.26405, 1.99597	27.96333, 2.47818
Exponential	6.38747	53.11015	24.83179
EV	7.80552, 2.95426	68.98744, 37.56619	30.47421, 12.91902

characteristics were on the right sides of the distributions. The skewness coefficients of the extreme parameter α_{max} were less than zero, which suggested that its heavy-tailed characteristic was on the left side of the distribution.

2) PARAMETER IDENTIFICATION OF DISTRIBUTION MODEL FOR ONE-DIMENSIONAL EXTREME PARAMETERS

According to multivariate copula theory, because $F_1(\beta_{max})$, $F_2(\Delta H_{max})$, and $F_3(\alpha_{max})$ are all continuous distribution functions, the three-dimensional copula function C in Eq.(3) is unique. Thus, to build a three-dimensional function C of the extreme parameters β_{max}, ΔH_{max}, and α_{max}, the generic distribution model for one-dimensional extreme parameters should be built first (shown in Eq.(1)). Six commonly used distribution models for one-dimensional extreme parameters are the generalized extreme value (GEV) distribution model (Eq.(16)), normal distribution model (Eq.(17)), lognormal distribution model (Eq.(18)), Weibull distribution model (Eq.(19)), exponential distribution model (Eq.(20)), and extreme value (EV) distribution model (Eq.(21)):

$$F(x; \mu, \sigma, \xi) = \exp\left\{-\left(1 + \xi \cdot \frac{x - \mu}{\sigma}\right)^{-1/\xi}\right\}, \quad (16)$$

$$F(x; \mu, \sigma) = \frac{1}{\sigma\sqrt{2\pi}} \int_{-\infty}^{x} \exp\left(-(t - \mu)^2 / 2\sigma^2\right) dt, \quad (17)$$

$$F(x; \mu, \sigma) = \frac{1}{\sigma\sqrt{2\pi}} \int_{0}^{x} \frac{e^{\frac{-(\ln(t)-\mu)^2}{2\sigma^2}}}{t} dt, \quad (18)$$

$$F(x; \mu, \sigma) = \int_{0}^{x} \sigma\mu^{-\sigma}t^{\sigma-1} \exp\left(-(t/\mu)^\sigma\right) dt, \quad (19)$$

$$F(x; \mu) = 1 - \exp(-x/\mu), \quad (20)$$

$$F(x; \mu, \sigma) = -\exp\left(-\exp\left(\frac{x-\mu}{\sigma}\right)\right), \quad (21)$$

where μ, σ, and ξ are all unknown parameters of the distribution models.

3) IDENTIFY UNKNOWN PARAMETERS AND TEST GOODNESS OF FIT

Based on the adaptive random particle optimization (ARPO) algorithm, the unknown parameters of the distribution models were all identified, as shown in Table 8. Figure 9 shows the

probability distribution histogram and cumulative probability distribution curves of the extreme parameters β_{max}, ΔH_{max}, and α_{max}. The results in Figure 9 suggest that the extreme parameter distribution is broadly consistent with the GEV, lognormal, and Weibull distribution models.

Figure 10 shows the quantile-quantile (QQ) plots of the extreme parameters β_{max}, ΔH_{max}, and α_{max}. As shown in Figure 10, the QQ plots of the GEV distribution model were almost straight lines, indicating that the probability distributions of the extreme parameters approximately formed the GEV distribution model. As shown in Table 9, the K-S test, A-D test, and χ^2 test of the extreme parameters also showed the same conclusion. The chi-squared value of the GEV distribution model was smaller than those of the other distributions, which indicated that the deviation between the probability distribution of the extreme parameters and the GEV distribution model was a minimum. Furthermore, the K-S and A-D values of the GEV distribution model were smaller than those of the other distributions. However, the P values of the GEV distribution model were larger than those of the other distributions, which indicated that the assumption that the probability distributions of the extreme parameters approximately formed GEV distributions passed the hypothesis test, at a far greater confidence level than 95%. In conclusion, the GEV distribution model could describe the extreme parameter distributions more effectively than the other models.

The GEV distribution model exhibited maximum stability [29], which meant that the distribution form of the normalized extreme parameters was consistent with the original distribution. Hence, the probability distribution functions $F_1(\beta_{max})$, $F_2(\Delta H_{max})$, and $F_3(\alpha_{max})$ were as follows (Eq.(22)–Eq.(24)), as shown at the bottom of the page 12. where $\bar{\beta}_{max}$, $\Delta\bar{H}_{max}$, and $\bar{\alpha}_{max}$ are the normalized values of the extreme parameters β_{max}, ΔH_{max}, and α_{max}, respectively, defined as follows:

$$\bar{\beta}_{max} = \frac{\beta_{max}}{\beta_c(W, Ma)}$$

$$\bar{\alpha}_{max} = \frac{\alpha_{max}}{\alpha_c(\delta_f, Ma)}$$

$$\Delta\bar{H}_{max} = \frac{\Delta H_{max}}{(450 - 38\sin\phi\cos\theta/2)}. \quad (25)$$

(a) Probability density diagram and cumulative probability density diagram of β_{max}

(b) Probability density diagram and cumulative probability density diagram of ΔH_{max}

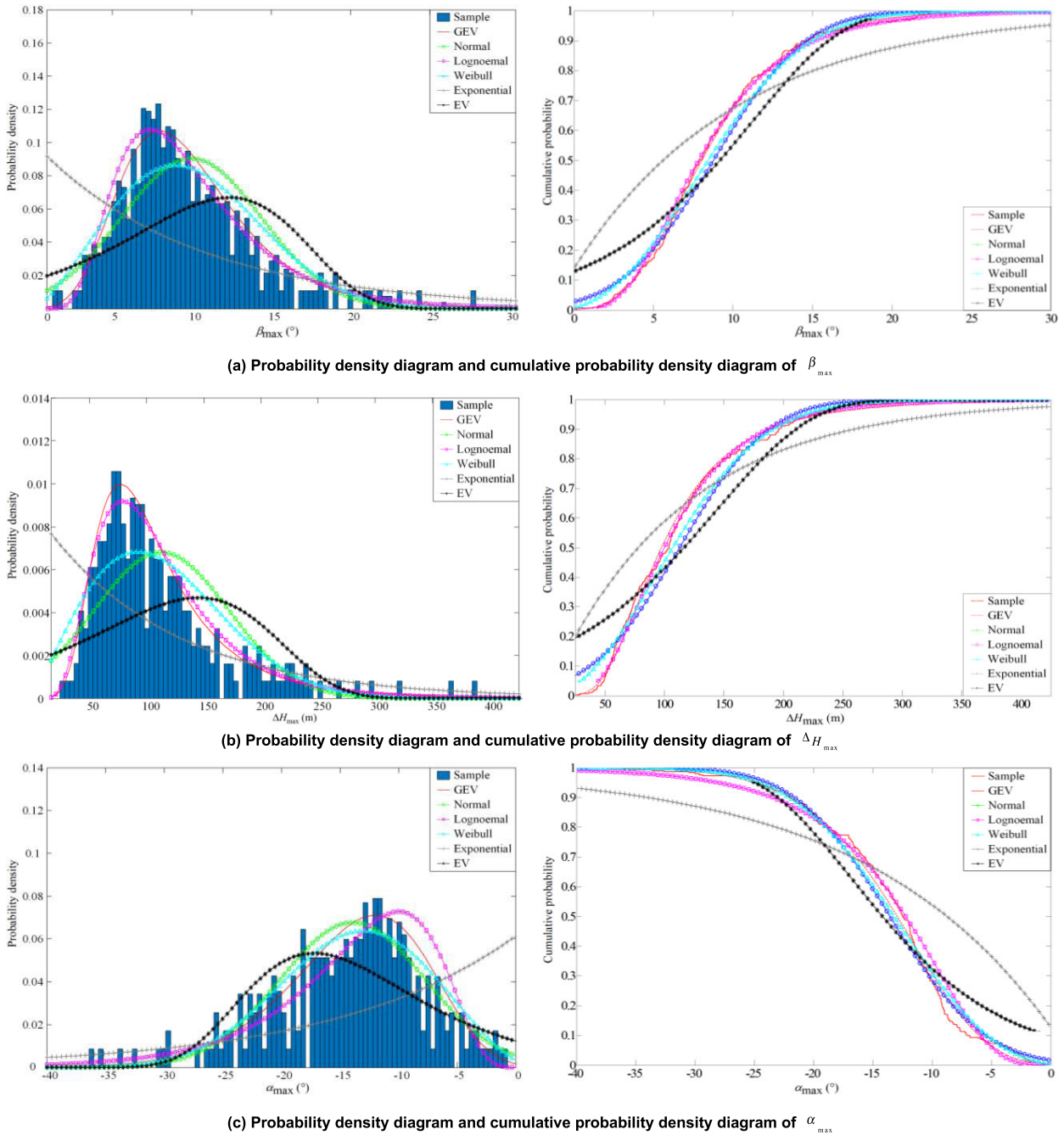(c) Probability density diagram and cumulative probability density diagram of α_{max}

FIGURE 9. Plot of the probability density and cumulative probability.

Eq.(25) is inserted into Eq.(13) to create a formula to judge the flight risk, as follows:

$$P_r = 1 \ if \ (\bar{\beta}_{max} > 1 \ or \ \Delta \bar{H}_{max} > 1 \ or \ \bar{\alpha}_{max} > 1). \quad (26)$$

B. IDENTIFY DISTRIBUTION MODEL OF THREE-DIMENSIONAL EXTREME PARAMETERS

1) PARAMETER IDENTIFICATION OF DISTRIBUTION MODEL FOR THREE-DIMENSIONAL EXTREME PARAMETERS

According to multivariate copula theory, the three-dimensional copula function C in Eq.(3) was unique, which describes the correlations between the three-dimensional parameters. Thus, to build the three-dimensional function C of the extreme parameters β_{max}, ΔH_{max}, and α_{max}, five commonly used distribution models for the three-dimensional extreme parameters were constructed: the Gumbel copula model (Eq. (27)), as shown at the bottom of the page 12, Frank copula model (Eq.(28)), as shown at the bottom of the page 12, GS copula model (Eq.(29)), as shown at the bottom of the page 12, Joe copula model (Eq.(30)), as shown at the bottom of the page 12, and FAWP copula model (Eq.(31)), as shown at the bottom of the page 12, where θ_i is an unknown parameter of the copula model.
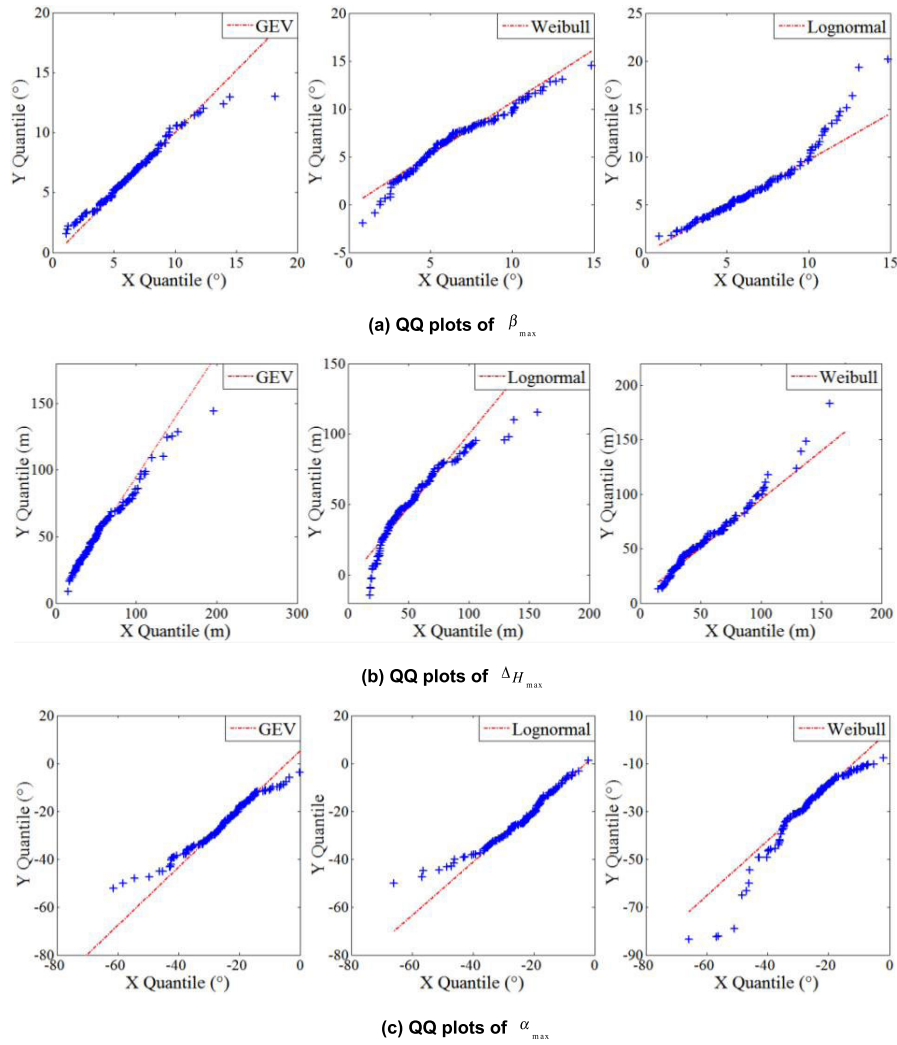
(a) QQ plots of $\beta_{\max}$

(b) QQ plots of $\Delta H_{\max}$

(c) QQ plots of $\alpha_{\max}$

FIGURE 10. QQ plots of extreme parameters.

TABLE 9. Goodness-of-fit test.

Function	Model	K-S	*P* Value	A-D	*P* Value	χ^2
F_1 $\beta_{\max}$	GEV	0.0600	0.9435	0.2574	0.9516	0.1043
	Lognormal	0.0800	0.7055	0.3582	0.5682	2.3861
	Weibull	0.0667	0.8820	2.6111	0.0765	0.3162
F_2 $\Delta H_{\max}$	GEV	0.0667	0.8820	0.4366	0.8116	0.2044
	Lognormal	0.0533	0.9804	0.4027	0.8458	0.2329
	Weibull	0.1067	0.3426	2.1391	0.0005	1.1707
F_3 $\alpha_{\max}$	GEV	0.0733	0.8000	0.4963	0.7503	0.3006
	Lognormal	0.1200	0.2155	1.8976	0.1047	1.7834
	Weibull	0.1133	0.2737	1.2393	0.0034	0.5942

Next, the one-dimensional probability distribution functions $F_1\left(\bar{\beta}_{\max}\right)$, $F_2\left(\bar{\alpha}_{\max}\right)$, and $F_3\left(\Delta\bar{H}_{\max}\right)$ are introduced to the five commonly used distribution models to build a three-dimensional function C and describe the correlations between the three-dimensional parameters.

2) IDENTIFY UNKNOWN PARAMETERS AND TEST GOODNESS OF FIT

Based on the ARPO algorithm, the unknown parameters of the distribution model were all identified, as shown in Table 10. Figure 11 shows the probability density map

TABLE 10. Identification results of the unknown parameters.

Copula model	Identification results
Gumbel Copula	1.159061,1.271576
Frank Copula	0.553232,0.982735
GS Copula	0.600121,1.179556
Joe Copula	0.9887,1.1420
FAWP Copula	$^-$1.296617,$^-$0.155644,$^-$1.235300,$^-$2.097956

FIGURE 11. Probability density plot of copula models.

of the three-dimensional copula function to illustrate the density characteristics of the copula models clearly. As shown in Figure 11, the Gumbel copula model, GS copula model, Joe copula model, and FAWP copula model possessed prominent heavy-tailed characteristics that could better describe the correlations between the three-dimensional extreme parameters.

Furthermore, based on the AIC, BIC, χ^2 test, and K-S test, the fitting results of the distribution were evaluated. As shown in Table 11, the Gumbel copula model, Joe copula model, and FAWP copula model had smaller AIC values, BIC values, χ^2 values, and K-S values than those of the other models. Furthermore, the values of the Gumbel copula model, Joe copula model, and FAWP copula model were all larger
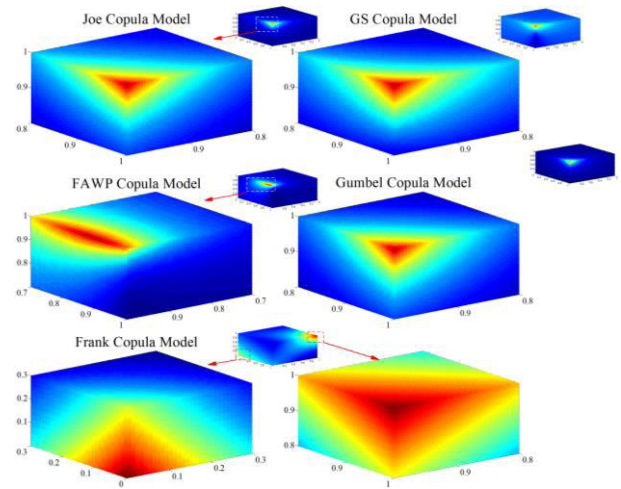
than the significance level of 0.05, which indicated that these three copulas passed the hypothesis test at the 95% confidence level. Hence, the Gumbel copula model, Joe copula model, and FAWP copula model are suitable models that can accurately describe the correlations between the three-dimensional parameters.

$$F_1(\bar{\beta}_{\max}; \mu, \sigma, \xi) = \exp\left\{-\left(1 - 0.08931 \cdot \frac{\bar{\beta}_{\max} - 5.22480}{2.32019}\right)^{1/0.08931}\right\}, \tag{22}$$

$$F_2(\Delta\bar{H}_{\max}; \mu, \sigma, \xi) = \exp\left\{-\left(1 + 0.21725 \cdot \frac{\Delta\bar{H}_{\max} - 38.60043}{17.71067}\right)^{-1/0.21725}\right\}, \tag{23}$$

$$F_3(\bar{\alpha}_{\max}; \mu, \sigma, \xi) = \exp\left\{-\left(1 - 0.07743 \cdot \frac{\bar{\alpha}_{\max} - 20.35252}{8.95829}\right)^{1/0.07743}\right\}, \tag{24}$$

$$C(u, v, w) = \exp\left(-\left\{(-\ln w)^{\theta_2} + \left[(-\ln u)^{\theta_1} + (-\ln v)^{\theta_1}\right]^{\frac{\theta_2}{\theta_1}}\right\}^{\frac{1}{\theta_2}}\right), \tag{27}$$

$$C(u, v, w) = -\frac{1}{\theta_2}\ln\left\{1 - \left(1 - e^{-\theta_2}\right)^{-1}\left(1 - e^{-\theta_2 w}\right)\left(1 - \left[1 - \left(1 - e^{-\theta_1}\right)^{-1}\left(1 - e^{-\theta_1 u}\right)\left(1 - e^{-\theta_1 v}\right)\right]^{\frac{\theta_2}{\theta_1}}\right)\right\}, \tag{28}$$

$$C(u, v, w) = \left\{1 + \left[\left(\frac{1}{w} - 1\right)^{\theta_2} + \left(\left(\frac{1}{u} - 1\right)^{\theta_1} + \left(\frac{1}{v} - 1\right)^{\theta_1}\right)^{\frac{\theta_2}{\theta_1}}\right]^{\frac{1}{\theta_2}}\right\}^{-1}, \tag{29}$$

$$C(u, v, w) = 1 - \left\{\left[(1 - u)^{\theta_1}\left(1 - (1 - v)^{\theta_1}\right) + (1 - v)^{\theta_1}\right]^{\frac{\theta_2}{\theta_1}}\left(1 - (1 - w)^{\theta_2}\right) + (1 - w)^{\theta_2}\right\}^{\frac{1}{\theta_2}}, \tag{30}$$

$$C(u, v, w) = uvw\exp\left[\left(\frac{\theta_1}{\ln u} + \frac{\theta_2}{\ln v}\right)^{-1}\right]\exp\left[\left(\frac{\theta_3}{\ln w} + \frac{\theta_4}{\ln u + \ln v + \left(\frac{\theta_1}{\ln u} + \frac{\theta_2}{\ln v}\right)^{-1}}\right)^{-1}\right]. \tag{31}$$

TABLE 11. Goodness-of-fit test.

Copula model	AIC	BIC	χ^2	K-S	P Value
Gumbel	-12.79700	-8.78348	0.6587	0.0939	0.2153
Frank	8.74035	3.72972	1.6574	0.2051	0.0484
GS	110.33880	114.04850	1.3426	0.2796	0.0084
Joe	-18.95536	-20.11106	0.5354	0.1028	0.3819
FAWP	-69.14397	-69.29643	0.3372	0.0735	0.4342

C. RISK-WEIGHTED MODEL

Based on the equation to judge the flight risk (Eq.(26)) and three-dimensional copula models, the results of the risk probability were obtained, as shown in Table 12.

TABLE 12. Risk probability.

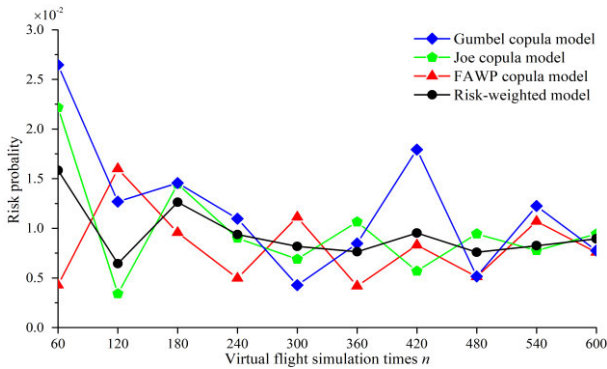| Copula model	Gumbel copula	Joe copula	FAWP copula
Risk probability	0.004268	0.00689	0.01112

FIGURE 12. Comparison of convergence between four models.

The difference in the risk probability value is not only related to the three-dimensional copula model, but also to virtual flight simulation times *n*, as shown in Figure 12. With the number of virtual flight simulation times increasing, the results of risk probability tend to be stable.

However, the computation ability of single computer is limited. In order to improve the efficiency of risk evaluation and reduce the number of virtual flight simulation times, the risk-weighted model was proposed.

$$P_r = W_{Gum} \cdot P_r^{Gum} + W_{Joe} \cdot P_r^{Joe} + W_{FAWP} \cdot P_r^{FAWP}. \quad (32)$$

where, the weight parameters W_{Gumbel}, W_{Joe}, and W_{FAWP} in the risk-weighted model were determined based on the P values from goodness-of-fit test, which were calculated using in Eq. (33).

$$W_i = P_i \bigg/ \sum_{i=1}^{3} P_i, \quad (33)$$

Figure 12 shows that the risk-weighted model is easily converged compared to other three copula models. and its risk evaluation accuracy approached stable when $n \geq 300$. Hence, the comprehensive risk probability P_r was calculated to be 0.00812342.

VI. RISK TOPOLOGY CONSTRUCTION OF FLIGHT MANIPULATION

A single and independent risk quantification value has little significance for risk management and control. Hence, based on the virtual landing simulation in the distributed human-machine-environment real-time simulation system, the risk topology of flight manipulation for landing in turbulent-windshear conditions was constructed using the pitch angle variation $\Delta\theta$, yaw angle variation $\Delta\psi$, and flight distance L by applying the quantitative risk evaluation method proposed in this study.

The process of the risk topology construction is illustrated in Figure 13, and operates with four steps as follows:
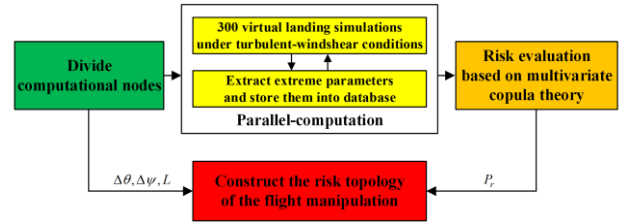

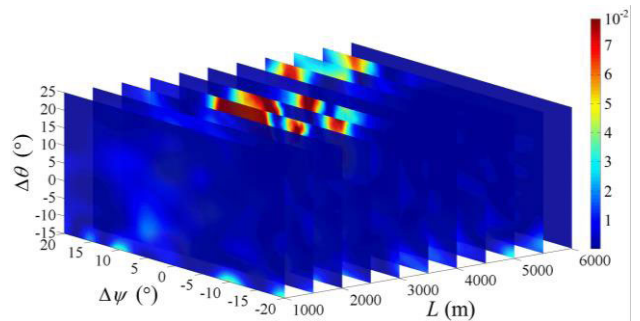**FIGURE 13.** Process of risk topology construction.

FIGURE 14. Three-dimensional risk topology of manipulation for landing in turbulent-windshear conditions.

Step 1: Divide computational nodes. The number of computational nodes in the risk topology was $40 \times 40 \times 60 = 96,000$, with pitch angle variation $\Delta\theta \in [-15° : 1° : 25°]$, yaw angle variation $\Delta\psi \in [-20° : 1° : 20°]$, and flight distance $L \in [0 : 100 : 6000]$. Each computational node corresponds to a flight manipulation situation.

Step 2: Parallel-computation. Each computational node is independent of the others, and so it is feasible to use the parallel-computation method to expedite the computational process. For each computational node, $n = 300$ virtual landing simulations were performed under turbulent-windshear conditions based on the distributed
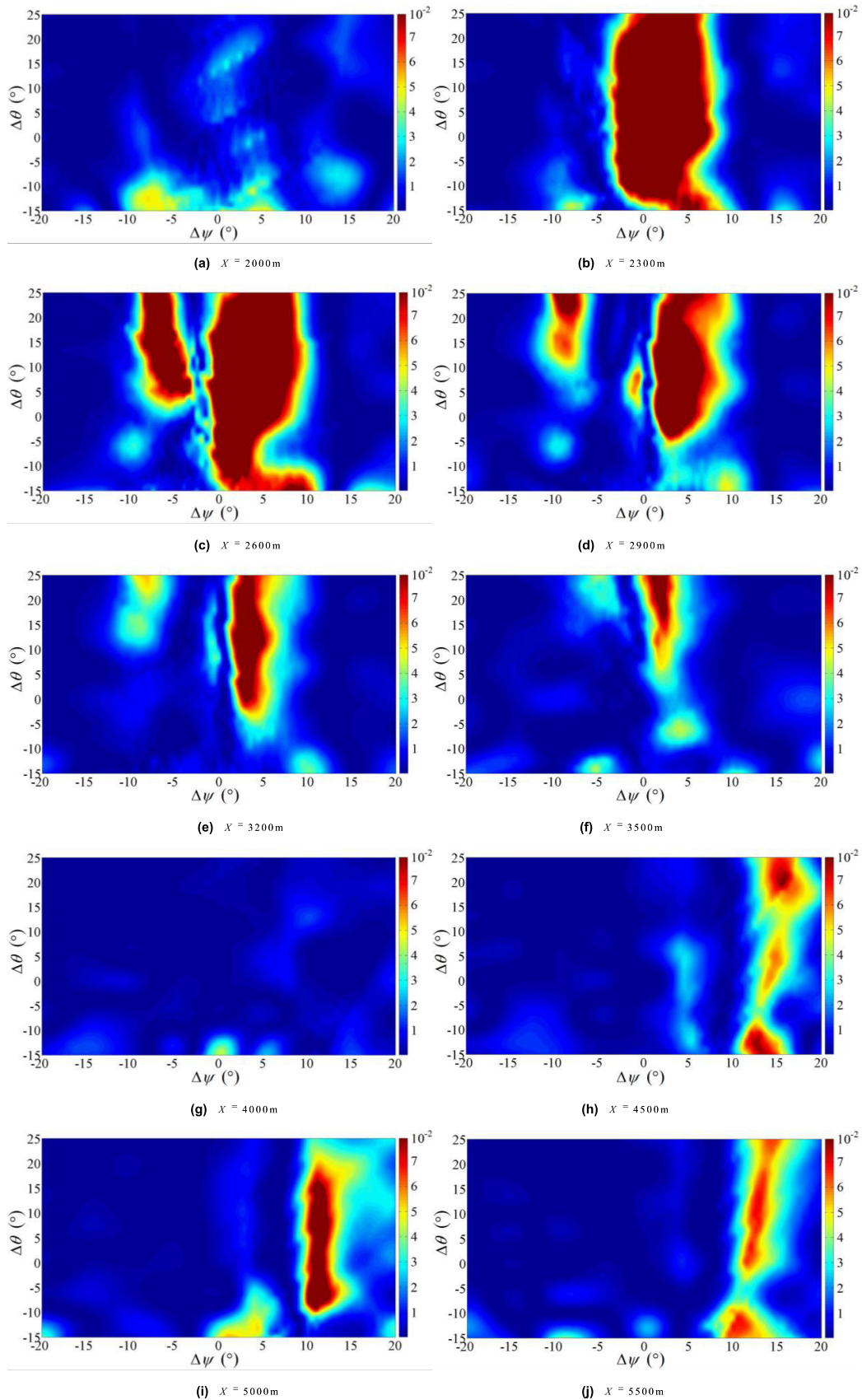
FIGURE 15. Two-dimensional risk topology of manipulation for landing when 2000 m $\leq X \leq$ 5500 m.

pilot-machine-environment real-time simulation system, and the extreme parameters $[\beta_{max}, H_{max}, \alpha_{max}]$ extracted from three hundred virtual landing simulations were stored into database as the evaluation data.

Step 3: Risk evaluation. The comprehensive risk probability P_r for all the computational nodes can be obtained based on multivariate copula theory accordingly.

Step 4: Construct the risk topology of flight manipulation. The risk topology is a three-dimensional (3-D) space formed by pitch angle variation $\Delta\theta$, yaw angle variation $\Delta\psi$, and flight distance L vectors, and the 3-D risk topology is dispersed by many computational nodes. Hence, the risk topology of flight manipulation was constructed in terms of the comprehensive risk probability values for all the computational nodes.

The risk topology of flight manipulation for landing in turbulent-windshear conditions was constructed, as shown in Figure 14. The risk topology can not only greatly improve the situational awareness of the pilot but also provide comprehensive and intuitive guidance to remove the aircraft from the impact of wind-shear.

Figure 15 shows the two-dimensional risk topology of flight manipulation for landing when $2000\,\text{m} \leq X \leq 5500\,\text{m}$. The risk-evolution mechanism of flight manipulation risk for landing in turbulent-windshear conditions is analyzed below.

Figure 15(a) shows the two-dimensional risk topology of flight manipulation when $X = 2000$ m. A negative pitch angle variation could lead to an increase in the risk probability, since the reduction of the effective angle of attack caused the loss of lift, which also affected the risk factor ΔH. Furthermore, the yaw angle variation $[-5°, 5°]$ means that the aircraft would enter the influence area of vortex 1 or 2 after Δt seconds, and risk factors α and ΔH would be both impacted. Hence, the aircraft must maintain a stable glide path in this stage. The pilot can adjust the track angle to align the aircraft with the runway and increase the pitch angle to decrease descent rate.

Figure 15(b) shows two-dimensional risk topology of flight manipulation when $X = 2300$ m. Because $\Gamma_2 > \Gamma_1$, the angle of attack would be impacted by vortex 2 first. The lift would decrease with the decrease in the angle of attack under its downdraft airflow influence, which would cause the risk factor ΔH to exceed the upper limit. An aircraft with inertia would enter the downwind area and the lift would further decrease. Due to the delay of emergency engine operation, the descent rate and angle of attack would both increase, which could lead to flight performance degradation. If the pilot failed to remove the aircraft from danger conditions, the aircraft would crash directly. This analysis revealed the significance of engine operation for removing the aircraft from dangerous conditions. Hence, the pilot should not excessively reduce the throttle to maintain a constant descent rate during landing. Furthermore, the pilot must coordinate the throttle and pitch angle based on experience and coordinate the relationship between the glide path and descent rate.

Figure 15(c) shows the two-dimensional risk topology of flight manipulation when $X = 2600$ m. Compared with Figure 15(b), the decrease in the right risk topology indicates that the impact of vortex 2 was still present but gradually weakened. The yaw angle variation $[-10°, 5°]$ meant that the aircraft entered the influence area of vortex 1 after Δt seconds, and a positive pitch angle variation would cause the angle of attack to exceed the stalling angle. The risk factors α and ΔH would be both impacted. It is noteworthy that a long and narrow security manipulation topology existed in the $\{(\Delta\psi, \Delta\theta)\,|3° < \Delta\psi < 4°, 8° < \Delta\theta < 25°\}$ range. This shows that it is possible for the aircraft to pass through the impact area of vortex 1 and vortex 2 and land securely.

Figure 15(e)-(g) shows that the impacts of vortex 1 and 2 gradually weakened, and the areas of risk topology gradually decreased. At this stage, the aircraft had a secure margin of flight manipulation. The pilot must pay more attention to the angle of attack and adjust the attitude of the aircraft to maintain a stable glide path over time.

Figure 15(h)-(j) shows that the impacts of vortex 3 gradually strengthened, and the areas of risk topology increased, because the risk factor β was impacted by vortex 3. The risk topology of flight manipulation indicated that the risk would rise sharply if the aircraft landed at a large yaw angle. At this stage, the pilot must pay more attention to the attitude of the aircraft and determine whether to pull up and go around based on their experience and capacity.

VII. CONCLUSION

By carrying out virtual landing simulations in the distributed human–machine–environment real-time simulation system, the risk topology of flight manipulation for landing in turbulent-windshear conditions was constructed which was composed of the pitch angle variation $\Delta\theta$, yaw angle variation $\Delta\psi$, and flight distance L based on the risk quantitative evaluation method proposed in this study. Furthermore, the risk-evolution mechanism of flight manipulation was analyzed in detail. The analysis led to the following conclusions:

1. It is dangerous to land in turbulent-windshear conditions. Multiple factors contributed to the risk. Hence, when the pilot lacks experience and ability, it is suggested that the process of landing in complex turbulent-windshear conditions be stopped at once. Unless airflow is smooth, the aircraft cannot land.

2. Flight manipulation in turbulent-windshear conditions is subject to multiple restrictions that are complex and variable. Due to the delayed effect of the stick and throttle, the aircraft handle quality and the flight performance may suddenly deteriorate. Hence, to ensure landing safety, it is necessary for the pilot to adopt appropriate training and accumulate manipulation experience.

3. The risk topology of flight manipulation is of great significance for improving the situational awareness of the pilot. The risk topology data under different conditions can be stored in an airborne computer in the form of a database. When the aircraft encounters different turbulent-windshear

conditions, the risk topology of flight manipulation can be quickly obtained by interpolation to provide the pilot with instructions.

In this study, the risk topology of flight manipulation in turbulent-windshear conditions was used as an example to discuss a risk topology construction method of flight manipulation. The accuracy of the risk topology is affected by many factors, so this study focused on the construction of a method to evaluate the risk and risk topology. The method and conclusions proposed in this study have reference significance and application value for landing safety assurance under turbulent-windshear conditions.

In addition, the proposed method can be used to verify the design of a flight control system and evaluate the flight performance and safety margin when the aircraft encounters various adverse conditions (such as complex environments and single engine failure).

REFERENCES

[1] *Human Performance, Enhancing Situational Awareness: FLT_OPS-HUM-PERF-SEQ 06-REV 01*, Airbus Customer Services, Blagnac, France, 2007.

[2] *Airplanes Statistical Summary of Commercial Jet Airplane Accidents: Worldwide Operations 1959–2012*, Boeing, Chicago, IL, USA, 2013.

[3] J. Che and D. Chen, "Automatic landing control using H∞ control and stable inversion," in *Proc. 40th IEEE Conf. Decis. Control*, Orlando, FL, USA, Dec. 2001, pp. 241–246.

[4] N. Botkin, V. Turova, J. Diepolder, M. Bittner, and F. Holzapfel, "Aircraft control during cruise flight in windshear conditions: Viability approach," *Dyn. Games Appl.*, vol. 7, no. 4, pp. 594–608, Dec. 2017.

[5] Z. Gao, J. Fu, and Y. Xu, "LPV robust suppresion control for fight in turbulent wind," in *Proc. 2nd IEEE Adv. Inf. Manage., Communicates, Electron. Autom. Control Conf. (IMCEC)*, Xi'an, China, May 2018, pp. 1–1705.

[6] V. J. Gawron and P. M. Jones, *Airplane Upset Training Evaluation Report*. Washington, DC, USA: NASA, 2002.

[7] B. Pei, H. Xu, and Y. Xue, "Flight-safety space and cause of incident under icing conditions," *J. Guid., Control, Dyn.*, vol. 40, no. 11, pp. 2983–2990, Nov. 2017.

[8] *IEEE Standard for Modeling and Simulation (M&S) High Level Architecture (HLA)-Framework and Rules*, IEEE Standard 1516, 2010.

[9] D. T. McRuer and E. S. Krendel, "Mathematical models of human pilot behavior", Paris, France: North Atlantic Treaty Organization, Advisory Group for Aerospace Research and Development, 1974, pp. 12–14.

[10] W. Frost, H.-P. Chang, K. Elmore, and J. Mccarthy, "Simulated flight through JAWS wind shear–In-depth analysis results," in *Proc. 22nd Aerosp. Sci. Meeting*, Reno, NV, USA, Jan. 1984, p. 276.

[11] M. Ivan, "A ring-vortex downburst model for flight simulations," *J. Aircr.*, vol. 23, no. 3, pp. 232–236, 1986.

[12] H. G. Visser, "Windshear recovery using thrust vectoring," *Aircr. Eng. Aerosp. Technol.*, vol. 71, no. 4, pp. 329–337, Aug. 1999.

[13] H. G. Visser, "Optimal lateral-escape maneuvers for microburst encounters during final approach," *J. Guid., Control, Dyn.*, vol. 17, no. 6, pp. 1234–1240, Nov. 1994.

[14] A. Dogan and P. T. Kabamba, "Microburst escape using altitude guidance," in *Proc. 37th IEEE Conf. Decis. Control*, Tampa, FL, USA, Dec. 1998, pp. 241–246.

[15] M. Lewis, K. Yenni, H. Verstynen, and L. Person, "Design and conduct of a windshear detection flight experiment," in *Proc. 6th AIAA Biennial Flight Test Conf.*, San Diego, CA, USA, Aug. 1992, pp. 4092–4097.

[16] Z. Zhao, Y. L. Xiao, and Y. J. Shi, "A digital simulation technique for dryden atmospheric turbulence model," *Chin. J. Aeronaut.*, vol. 1, no. 2, pp. 89–97, Jul. 1988.

[17] W. T. Cui, W. H. Liu, and X. Y. Lei, "Modeling and simulation of microburst wind shear in the flight simulator," in *Proc. IEEE Chin. Guid., Navigat. Control Conf.*, Yantai, China, Aug. 2014, pp. 1095–1100.

[18] J. V. Rosenberg and T. Schuermann, "A general approach to integrated risk management with skewed, fat-tailed risks," *J. Financial Econ.*, vol. 79, no. 3, pp. 569–614, Mar. 2006.

[19] L.-C. Ho, P. Burridge, J. Cadle, and M. Theobald, "Value-at-risk: Applying the extreme value approach to asian markets in the recent financial turmoil," *Pacific-Basin Finance J.*, vol. 8, no. 2, pp. 249–275, May 2000.

[20] M. Dithinde, K. K. Phoon, M. De Wet, and J. V. Retief, "Characterization of model uncertainty in the static pile design formula," *J. Geotechnical Geoenvironmental Eng.*, vol. 137, no. 1, pp. 70–85, Jan. 2011.

[21] E. Jondeau and M. Rockinger, "Conditional dependency of financial series: The copula-GARCH model," FAME Res. Paper 69, Dec. 2002.

[22] S. Ghosh, "Modelling bivariate rainfall distribution and generating bivariate correlated rainfall data in neighbouring meteorological subdivisions using copula," *Hydrological Processes*, vol. 24, no. 24, pp. 3558–3567, Nov. 2010.

[23] S. Coles, J. Bawa, L. Trenner, and P. Dorazio, *An Introduction to Statistical Modeling of Extreme Values*. New York, NY, USA: Springer, 2001, pp. 45–73.

[24] L. De Haan and A. Ferreira, *Extreme Value Theory: An Introduction*. New York, NY, USA: Springer, 2006, pp. 65–126.

[25] L. Wang, X. Guo, J. Zeng, and Y. Hong, "Using Gumbel copula and empirical marginal distribution in estimation of distribution algorithm," in *Proc. 3rd Int. Workshop Adv. Comput. Intell.*, Suzhou, China, Aug. 2010, pp. 583–587.

[26] B. De Baets and H. De Meyer, "On a conjecture about the frank copula family," *Fuzzy Sets Syst.*, vol. 228, pp. 15–28, Oct. 2013.

[27] J. Huo, R. Zhang, Z. Tai, X. Dong, and D. O. Mathematics, "Research on dependency of financial markets based on Eviews and GS Copula function," *J. Jilin Univ.*, vol. 33, no. 6, pp. 690–698, Nov. 2015.

[28] Y. Xue, H.-J. Xu, and X.-L. Wang, "Build probability distribution maps of flight risk during wake encountering," *J. Aircr.*, vol. 52, no. 3, pp. 805–818, May 2015.

[29] Q. Li, "The study of financial market risk measurement based on copula theory and GPD model," Ph.D. dissertation, Dept. Manag. Eng, Chongqing Univ., Chongqing, China, 2012.

[30] H. Fang, N. Tian, Y. Wang, M. Zhou, and M. A. Haile, "Nonlinear Bayesian estimation: From Kalman filtering to a broader horizon," *IEEE/CAA J. Automatica Sinica*, vol. 5, no. 2, pp. 401–417, Mar. 2018.

[31] S. Gao, M. Zhou, Y. Wang, J. Cheng, H. Yachi, and J. Wang, "Dendritic neuron model with effective learning algorithms for classification, approximation, and prediction," *IEEE Trans. Neural Netw. Learn. Syst.*, vol. 30, no. 2, pp. 601–614, Feb. 2019.

[32] T. Zhou, S. Gao, J. Wang, C. Chu, Y. Todo, and Z. Tang, "Financial time series prediction using a dendritic neuron model," *Knowl.-Based Syst.*, vol. 105, pp. 214–224, Aug. 2016.

[33] K. D. Do, "Stability in probability and inverse optimal control of evolution systems driven by levy processes," *IEEE/CAA J. Automatica Sinica*, vol. 7, no. 2, pp. 405–419, Mar. 2020.

[34] S. Li, R. He, B. Lin, and F. Sun, "DOA estimation based on sparse representation of the fractional lower order statistics in impulsive noise," *IEEE/CAA J. Automatica Sinica*, vol. 5, no. 4, pp. 860–868, Jul. 2018.

GUOZHI WANG was born in Shandong, China, in 1995. He received the B.E. degree from Air Force Engineering University, China, in 2017, where he is currently pursuing the Ph.D. degree in aeronautical and astronautical science and technology. His research interest includes flight risk evaluation.

HAOJUN XU was born in Zhejiang, China, in 1965. He received the B.E. and M.E. degrees from Air Force Engineering University, China, in 1986 and 1989, respectively. He is currently a Full Professor with the Aeronautics Engineering College, Air Force Engineering University.

BINBIN PEI was born in Anhui, China, in 1990. He received the B.E. and Ph.D. degrees from Air Force Engineering University, China, in 2014 and 2018, respectively. He is currently a Lecturer with the Aeronautics Engineering College, Air Force Engineering University.

XIAOCONG DUAN was born in Anhui, China, in 1995. He received the B.E. degree from Air Force Engineering University, China, in 2018, where he is currently pursuing the M.E. degree. His research interest includes flight simulation.

YUAN XUE was born in Shandong, China, in 1986. He received the B.E. and Ph.D. degrees from Air Force Engineering University, China, in 2008 and 2013, respectively. He is currently a Lecturer with the Aeronautics Engineering College, Air Force Engineering University.